



UNIVERSITY OF LEEDS

This is a repository copy of *Automated Retinal Lesion Detection via Image Saliency Analysis*.

White Rose Research Online URL for this paper:
<http://eprints.whiterose.ac.uk/151446/>

Version: Accepted Version

Article:

Yan, Q, Zhao, Y, Zheng, Y et al. (4 more authors) (2019) Automated Retinal Lesion Detection via Image Saliency Analysis. *Medical Physics*, 46 (10). pp. 4531-4544. ISSN 0094-2405

<https://doi.org/10.1002/mp.13746>

© 2019 American Association of Physicists in Medicine. This is an author produced version of a paper published in *Medical Physics*. Uploaded in accordance with the publisher's self-archiving policy.

Reuse

Items deposited in White Rose Research Online are protected by copyright, with all rights reserved unless indicated otherwise. They may be downloaded and/or printed for private study, or other acts as permitted by national copyright laws. The publisher or other rights holders may allow further reproduction and re-use of the full text version. This is indicated by the licence information on the White Rose Research Online record for the item.

Takedown

If you consider content in White Rose Research Online to be in breach of UK law, please notify us by emailing eprints@whiterose.ac.uk including the URL of the record and the reason for the withdrawal request.



eprints@whiterose.ac.uk
<https://eprints.whiterose.ac.uk/>

Automated Retinal Lesion Detection via Image Saliency Analysis

Qifeng Yan^{1,2}, Yitian Zhao^{2*}, Yalin Zheng^{2,3}, Yonghuai Liu⁴, Kang Zhou^{2,5}, Alejandro Frangi^{2,6}, Jiang Liu^{2,7}

1 University of Chinese Academy of Sciences, Beijing, 100049, China.

2 Cixi Institute of Biomedical Engineering, Ningbo Institute of Materials Technology and Engineering, Chinese Academy of Sciences, Cixi, 315399, China.

3 Department of Eye and Vision Science, University of Liverpool, Liverpool, L7 8TX, UK

4 Department of Computer Science, Edge Hill University, Ormskirk, L39 4QP, UK

5 School of Information Science and Technology, ShanghaiTech University, Shanghai, 201210, China.

6 School of Computing, University of Leeds, Leeds, S2 9JT, UK.

7 Department of Computer Science and Engineering, Southern University of Science and Technology, Shenzhen, 518055, China.

* E-mail: yitian.zhao@nimte.ac.cn

Abstract

Background and Objective: The detection of abnormalities such as lesions or leakage from retinal images is an important health informatics task for automated early diagnosis of diabetic and malarial retinopathy or other eye diseases, in order to prevent blindness and common systematic conditions. In this work, we propose a novel retinal lesion detection method by adapting the concepts of saliency. **Methods:** Retinal images are firstly segmented as superpixels, two new saliency feature representations: *uniqueness* and *compactness*, are then derived to represent the superpixels. The pixel level saliency is then estimated from these superpixel saliency values via a bilateral filter. These extracted saliency features form a matrix for low-rank analysis to achieve saliency detection. The precise contour of a lesion is finally extracted from the generated saliency map after removing confounding structures such as blood vessels, the optic disc, and the fovea. The main novelty of this method is that it is an effective tool for detecting different abnormalities at pixel-level from different modalities of retinal images, without the need to tune parameters. **Results:** To evaluate its effectiveness, we have applied our method to seven public datasets of diabetic and malarial retinopathy with four different types of lesions: exudate, hemorrhage, microaneurysms, and leakage. The

32 evaluation was undertaken at pixel-level, lesion-level, or image-level according to ground truth
33 availability in these datasets. **Conclusions:** The experimental results show that the proposed
34 method outperforms existing state-of-the-art ones in applicability, effectiveness, and accuracy.

35 **Keywords:** Saliency, feature, low-rank, retinal image, lesion detection

1 Introduction

The human retina is a window that allows clinicians to study retinal conditions such as diabetic retinopathy (DR) [1] and malarial retinopathy (MR) [2] as well as other systematic conditions such as cardiovascular diseases and stroke with non-invasive imaging techniques due to its transparency in nature. In particular, DR is a leading cause of vision impairment and loss in the working-age population [3] which affects nearly 500 million of people with diabetes worldwide. The severity of DR is usually determined by identifying specific features, such as exudates (EX), microaneurysms (MA), and hemorrhages (HE) in retinal color fundus (CF) images. MR has been identified as an important clinical sign in the diagnosis and prognosis of cerebral malaria (CM), which is still a major cause of death and disability in children in sub-Saharan Africa. Leakage (LK) in fluorescein angiogram (FA) is an important sign in determining the activity and development of lesions of MR [2]. Figure 1 shows these four types of anomalies in MR and DR respectively. The automated detection of these pathologies from retinal images is important in understanding the mechanism, diagnosis, optimal treatment and surgical planning in tackling retinal diseases.

Current practical approaches for the quantitative analysis of retinal abnormalities require extensive manual annotation by experienced graders [4]. Manual grading is often time-consuming, expensive and subject to human errors, thus will be impractical for routine clinical applications. To overcome these limitations, cost-effective solutions will rely on automatic identification of suspicious regions by computer-aided diagnosis systems [1, 5].

In this work, the candidate lesion regions in given retinal images are treated as ‘salient’ and determined by using a low-rank analysis-based method [6]. *Saliency* usually means that an area stands out relative to its neighbors for its uniqueness or rarity features [7, 8]. In the field of medical image analysis, saliency can describe suspected regions that contain indicative signs for diagnostic purposes, and will always command the attention of human experts [9]. Low-rank analysis has shown great potential for the detection of saliency [6, 10, 11]. Those parts with redundant information of an image usually show high regularities and lie in a low dimensional feature subspace. This can be approximated as a low-rank feature matrix. The salient part can be viewed as a sparse matrix [6]. To form the matrix for the low-rank analysis, a novel UNICOM feature is proposed, which seamlessly integrate UNIqueness and COMpactness features) for the

65 representation of superpixels in images. The proposed framework for retinal lesion detection is a
66 substantial extension to our previous work published in MICCAI-2018 [12] where only a uniqueness-
67 based feature was proposed. In this work, the previous uniqueness-based feature is combined with
68 a new compactness-based feature to form an integrated UNICOM feature, as the key input to the
69 feature matrix of the given image for the subsequent low rank based saliency analysis. In essence,
70 the uniqueness-based feature evaluates the rarity of image components whilst the compactness-
71 based feature is a complementary feature to intensity for saliency description, to reduce the number
72 of falsely-detected salient regions. Figure 2 illustrates the performance of the proposed framework
73 on detecting salient regions of a retinal image. In identifying high-level contextual features and
74 seeking to emulate human cognitive processes, the proposed method extracts EX, MA and HE at
75 pixel level in retinal color fundus images, and LK in FA. In line with [13], MA and HE are called
76 dark lesions and EX and LK as bright lesions during evaluating our work.

77 The main contributions of this paper can be summarized as follows. **(i)** We have proposed
78 a novel adaption of the concepts of saliency and low-rank analysis to the field of retinal image
79 analysis. **(ii)** A novel UNICOM feature is extracted for the representation of an image and form
80 a matrix for low-rank analysis. **(iii)** The proposed method has undergone rigorous quantitative
81 evaluation using seven publicly-available datasets including CF and FA images with four different
82 types of retinal abnormalities. The results show that our method is more accurate and robust to
83 variations in the location, size, intensity, inhomogeneity and modality of the data than the selected
84 state-of-the-art ones for lesion detection.

85 2 Related Works

86 In recent years, developing health informatics systems for computer aided screening and grading of
87 retinal diseases has received increasing attention, as evidenced by extensive reviews [5, 14], and the
88 Diabetic Retinopathy: Segmentation and Grading Challenge at IEEE International Symposium
89 on Biomedical Imaging (ISBI-2018)¹.

90 Existing methods rely on identifying suspected lesions from the analysis of fundus images, and
91 they can be categorized into three groups based on their ability to detect different types of lesion:

¹<https://idrid.grand-challenge.org/Home/>

92 **i)** dark lesions such as MA and HE, **ii)** bright lesions such as EX and LK, and **iii)** combined dark
93 and bright lesions.

94 *Dark lesion detection.* Fleming et al. [15] proposed an automated MA detection method using
95 local contrast normalization and local vessel detection. A hybrid approach consisting of mathe-
96 matical morphology and k-Nearest Neighbors (kNN) classification was introduced by Niemeijer et
97 al. [1] for the MA extraction. Giancardo et al. [16] utilized a thresholding technique followed by
98 a Radon transformation and support vector machine (SVM) for MA detection. Tang et al. [17]
99 presented a splat feature classification method to detect retinal HE. This classification can model
100 shapes of various lesions efficiently regardless of their variability in appearance, texture or size. A
101 multi-agent system was proposed in [18] which uses gradient patterns and Gaussian fitting param-
102 eters in different directions to segment MA. Dai et al. [19] employed gradient vector analysis and
103 a class-imbalance classifier to determine MA candidates. Seoud et al. [3] generated a new set of
104 shape features called Dynamic Shape Features to detect dark lesions from retinal images. Dasht-
105 bozorg et al. [4] used a gradient weighting-based iterative thresholding approach and a boosting
106 classifier to locate MA.

107 *Bright lesion detection.* Phillips et al. [20] calculated the gradient of intensity, and then
108 thresholded the gradient values to determine LK regions in DR images. In [21], the EX contours
109 were determined by means of morphological reconstruction techniques. Sanchez et al. [22, 23] used
110 a statistical technique called mixture model and contextual information to detect the EX. Welfer
111 et al. [24] employed a coarse-to-fine strategy for detecting EX in retinal images. In [25], a set of
112 features based on color, wavelet decomposition and automatic lesion segmentation were employed to
113 train a classifier, which is able to detect EX in color fundus images. Agurto et al. [26] proposed an
114 EX detection method based on optimal thresholding of instantaneous amplitude, and a partial least
115 squares-based classification. Rabbani et al.[27] employed an active contour segmentation model
116 to detect the boundaries of LK in FA images of subjects with diabetic macular edema. Zhao et
117 al. [28] used the intensity and compactness features to generate a saliency map, and segment the
118 precise LK area by using a graph-cut model. Liu et al. [29] presented a location-to-segmentation
119 strategy for automatic EX segmentation in color retinal fundus images.

120 *Combined bright and dark lesion detection.* A visual word dictionary-based feature detection
121 and analysis framework was proposed by Rocha et al. [30], which is capable of identifying MA

122 and EX. Roychowdhury et al. [13] designed a system called DREAM for the grading of DR using
123 machine learning. Non-lesions, or false positives, are rejected by the hierarchical classification, and
124 the lesions are classified into bright and dark ones by using multiple classification criteria. Zhang
125 et al. [31] proposed a multi-scale correlation coefficients-based method and a dynamic thresholding
126 technique for retinal lesion extraction. A rule-based classification and dictionary learning algorithm
127 was then employed for more accurate detection of retinal lesions. Gondal et al. [32] proposed to
128 use a modified Convolutional Neural Network (CNN) in weak supervision with only image-level
129 labels to identify lesions. Quellec et al. [33] generated a heat map as a key input for their deep
130 learning approach - ConvNets. This network can be utilized for DR screening, and both bright
131 and dark lesions are detected at the image level and at the lesion level respectively. However, as a
132 deep learning technique this method is data hungry and limited by the data availability.

133 The majority of previous approaches to lesion detection are based solely on morphological
134 segmentation or classification [15, 16, 17, 19, 21, 13, 33, 32]. These strategies usually work on a
135 single type of lesions with careful parameter optimization and training data collection, but often
136 fail to work for the detection of other types of lesions without problem-specific optimization or
137 information. It is therefore essential to develop generic algorithms with accurate and reliable
138 performance for the detection of different types of lesions without over-relying on the need of
139 handcrafted parameters or knowledge.

140 **3 Proposed method**

141 In this section, we detail our novel UNICOM feature based saliency detection model for retinal
142 lesion detection. The main steps of our approach are illustrated in Figure 3. The details of these
143 steps are described in these four subsections.

144 **3.1 UNICOM saliency feature**

145 Finding a good discriminative feature plays a key role in ensuring the validity of the saliency
146 detection model. In this work, we propose a novel feature: the UNICOM, which combines intensity
147 uniqueness and spatial compactness characteristics.

148 Perazzi et al. [34] suggest that the *uniqueness* of a component may reveal the rarity of an image

149 component. Relative intensity is a commonly used property in the investigation of saliency [34]:
 150 salient regions stand out from their surroundings in certain aspects. Cheng et al. [35] suggest that
 151 *compactness* can measure elemental distribution. These elements are more salient when they are
 152 grouped in a particular image region rather than evenly distributed over the whole image.

Inspired by the fact that human vision is usually more concerned with objects than with individual pixels and the objects of interest may vary in size, in this paper an input image is firstly partitioned into N superpixels $\{P_i\}_{i=1}^N$, by using the Simple Linear Iterative Clustering (SLIC) method [36]. Without loss of generality, we assume that N superpixels are generated, the colors of any two superpixels i and j , $1 \leq i, j \leq N$, are \mathbf{c}_i and \mathbf{c}_j , while their positions are \mathbf{p}_i and \mathbf{p}_j . The UNICOM feature U_i of superpixel i is then defined by combining the uniqueness of intensity \mathcal{I} and the compactness of spatial distribution \mathcal{D} :

$$\mathbf{U}_i = \mathcal{I}_i \cdot \exp(-k \cdot \mathcal{D}_i), \quad (1)$$

153 where an exponential function is employed to emphasize \mathcal{D}_i , which is of higher significance and
 154 greater diagnostic capability than the intensity measurement \mathcal{I}_i [34]. The parameter k represents
 155 the strength of the spatial weighting, and is set as 6 and -6 for dark and bright lesion detection,
 156 respectively.

157 3.1.1 Uniqueness feature generation

The uniqueness in the intensity domain I_i of superpixel i is estimated by computing the rarity compared to all the other superpixels j :

$$\mathcal{I}_i = \sum_{j=1, j \neq i}^N \|\mathbf{c}_i - \mathbf{c}_j\|^2 \cdot w^I(\mathbf{p}_i, \mathbf{p}_j). \quad (2)$$

where \mathbf{c} indicates the intensity value. The local weighting function $w^I(\mathbf{p}_i, \mathbf{p}_j)$ is introduced here so that global and local contrast can be effectively combined with control over the influence radius. A standard Gaussian function is utilized to model the local contrast in terms of geometric distances

between superpixels i and j :

$$w^I(\mathbf{p}_i, \mathbf{p}_j) = \frac{1}{\mathbf{Z}_i^I} \exp\left\{-\frac{\|\mathbf{p}_i - \mathbf{p}_j\|^2}{2\sigma_p^2}\right\}, \quad (3)$$

where standard deviation σ_p controls the range of the uniqueness operator from 0 to 1 (where 1 = global uniqueness) and was empirically set to 0.8. The normalization term \mathbf{Z}_i^I ensures that $\sum_{j=1, j \neq i}^N w^I(\mathbf{p}_i, \mathbf{p}_j) = 1$. Eqn.2 can be decomposed by factoring out:

$$\begin{aligned} \mathcal{I}_i &= \mathbf{c}_i^2 \underbrace{\sum_{j=1, j \neq i}^N w^I(\mathbf{p}_i, \mathbf{p}_j)}_1 \\ &\quad - 2\mathbf{c}_j \underbrace{\sum_{j=1, j \neq i}^N \mathbf{c}_j w^I(\mathbf{p}_i, \mathbf{p}_j)}_{\text{Gaussian blur } \mathbf{c}_j} + \underbrace{\sum_{j=1, j \neq i}^N \mathbf{c}_j^2 w^I(\mathbf{p}_i, \mathbf{p}_j)}_{\text{Gaussian blur } \mathbf{c}_j^2}. \end{aligned} \quad (4)$$

158 It can be seen from Eqn.4 that both terms $\sum_{j=1, j \neq i}^N \mathbf{c}_j w^I(\mathbf{p}_i, \mathbf{p}_j)$ and $\sum_{j=1, j \neq i}^N \mathbf{c}_j^2 w^I(\mathbf{p}_i, \mathbf{p}_j)$ can
 159 be regarded as the Gaussian blurring kernel on intensities \mathbf{c}_j and their squares \mathbf{c}_j^2 , respectively.
 160 Figure 3 (b) depicts an example of the proposed uniqueness-based feature.

161 3.1.2 Compactness feature generation

Cheng et al.[35] suggest that spatial variance is a potential measure of an element's distribution. Low variance of its compactness implies that an element should be considered more salient than one that is spatially more widely distributed. The human visual system tends to pay more attention to a more compact object than to a more diffuse object [6, 28]. The measure of compactness of an object might therefore be of use as a complementary feature to intensity for saliency analysis. Similarly, the compactness of spatial distribution \mathcal{D}_i is estimated as:

$$\mathcal{D}_i = \sum_{j=1, j \neq i}^N \|\mathbf{p}_j - \mu_i\|^2 \cdot w^D(\mathbf{c}_i, \mathbf{c}_j), \quad (5)$$

where $\mu_i = \sum_{j=1, j \neq i}^N \mathbf{p}_j w^D(\mathbf{c}_i, \mathbf{c}_j)$ defines the weighted mean position of positions \mathbf{p}_j , and $w^D(\mathbf{c}_i, \mathbf{c}_j)$ indicates the degree of similarity between colors \mathbf{c}_i and \mathbf{c}_j . As in Eqn.2, the color similarity weight is also estimated using a Gaussian function $w^D(\mathbf{c}_i, \mathbf{c}_j) = \frac{1}{\mathbf{Z}_i^D} \exp\left\{-\frac{\|\mathbf{c}_i - \mathbf{c}_j\|^2}{2\sigma_c^2}\right\}$, where \mathbf{Z}_i^D can be

defined as to \mathbf{Z}_i^f , while σ_c controls the sensitivity of the spatial distribution: larger values of σ_c indicate increased values of spatial distribution, and vice versa. It was also empirically set to 0.8.

Eqn.5 can be expanded as:

$$\begin{aligned}
 \mathcal{D}_i &= \sum_{j=1, j \neq i}^N \mathbf{p}_j^2 w^D(\mathbf{c}_i, \mathbf{c}_j) \\
 &\quad - 2\mu_i \underbrace{\sum_{j=1, j \neq i}^N \mathbf{p}_j w^D(\mathbf{c}_i, \mathbf{c}_j)}_{\mu_i} + \mu_i^2 \underbrace{\sum_{j=1, j \neq i}^N w^D(\mathbf{c}_i, \mathbf{c}_j)}_1 \\
 &= \underbrace{\sum_{j=1, j \neq i}^N \mathbf{p}_j^2 w^D(\mathbf{c}_i, \mathbf{c}_j)}_{\text{Gaussian blur } \mathbf{p}_j^2} - \underbrace{\mu_i^2}_{\text{Gaussian blur } \mathbf{p}_j}.
 \end{aligned} \tag{6}$$

162 Again, both terms $\sum_{j=1, j \neq i}^N \mathbf{p}_j w^D(\mathbf{c}_i, \mathbf{c}_j)$ and μ_i^2 can be effectively treated as Gaussian blurring.
 163 It will be observed that the more distinct superpixel i is from superpixel j , the larger the value of
 164 \mathcal{D}_i , and vice versa. Figure 3 (c) shows an example of the proposed compactness-based feature.

165 By incorporating the compactness feature \mathcal{D}_i with the uniqueness feature \mathcal{I}_i of a given image,
 166 the UNICOM feature \mathbf{U}_i is calculated using Eqn.1.

167 3.2 Saliency detection

168 Low-rank and sparsity analysis provides a useful tool for detecting salient regions [6]. A region with
 169 high regularities (redundancy or background) usually lies in a low dimensional feature subspace,
 170 which can be approximated as a low-rank feature matrix, while a salient region can be represented
 171 by a sparse feature matrix. The term *sparsity* shares some similarities with the perception of
 172 *contrast*, which implies that the pixels or regions differ significantly from their surroundings. The
 173 relation between sparsity and saliency follows the fact that only distinctive sensory information is
 174 selected for further processing in a human vision system.

175 D -dimension features are extracted from each superpixel including the above-obtained UNI-
 176 COM feature, and the stacked feature vectors form a matrix representation of the input image as
 177 $\mathbf{F} = [f_1, f_2, \dots, f_N] \in \mathbb{R}^{D \times N}$. In this work, 31 features were used to form the feature matrix, and
 178 the feature details and importance of these features will be listed and discussed in Sec. VI. C.

The saliency detection task may then be further modeled as a low-rank matrix recovery problem

[37]:

$$\min_{\mathbf{L}, \mathbf{S}} \text{rank}(\mathbf{L}) + \lambda \|\mathbf{S}\|_0 \quad \text{s.t.} \quad \mathbf{F} = \mathbf{L} + \mathbf{S}, \quad (7)$$

where $\|\cdot\|_0$ denotes the l_0 -norm, and \mathbf{L} is the low-rank matrix corresponding to the background. This suggests that matrix \mathbf{L} may have the property of low-rankness. \mathbf{S} is the sparse matrix representing the salient parts, and these usually display characteristic and spatial coherence. Since such a problem takes non-deterministic polynomial time[37], one can alternatively solve its convex surrogate instead for computational efficiency and feasibility:

$$\min_{\mathbf{L}, \mathbf{S}} \|\mathbf{L}\|_* + \lambda \|\mathbf{S}\|_1 \quad \text{s.t.} \quad \mathbf{F} = \mathbf{L} + \mathbf{S}, \quad (8)$$

179 where $\|\cdot\|_*$ and $\|\cdot\|_1$ denote the nuclear norm and l_1 -norm of \mathbf{L} and \mathbf{S} , respectively. Various
 180 algorithms that can be used to estimate the sparse matrix \mathbf{S} , and the Robust Principal Component
 181 Analysis (Robust PCA) [38, 37] is a powerful tool to recover the decomposed low-rank \mathbf{L} and sparse
 182 \mathbf{S} matrices. We refer to [37] for more details on Robust PCA. The saliency map is generated by
 183 assembling the l_1 -norm of each column S_i in \mathbf{S} from the corresponding segments, and further
 184 normalized into grayscale for display and visualization.

185 In medical image analysis, uniformly sampled patches often display large feature variations,
 186 such as a high degree of anatomical variation across the population and the complexity of the
 187 surrounding tissue/organs, and these characteristics may affect the accuracy of saliency detection.
 188 On one hand, some generated patches may contain both background and salient regions, and this
 189 may lead to an invalid assumption that the background has a low-rank. On the other hand, if the
 190 salient region is large, it may be decomposed into many patches, and these fragmented patches
 191 will then not be salient because they are no longer identified as sparse.

Decomposing \mathbf{F} in the original feature space usually produces inferior saliency detection results, as the sparse analysis only ensures that a single patch is encoded as a sparse vector, which may not correspond to the saliency over the entire image. The authors of [6] instead trained a linear transformation matrix \mathbf{T} on the feature space from a set of training images:

$$\min_{\mathbf{L}, \mathbf{S}} \|\mathbf{L}\|_* + \lambda \|\mathbf{S}\|_1 \quad \text{s.t.} \quad \mathbf{TF} = \mathbf{L} + \mathbf{S}. \quad (9)$$

192 In this new space, the variation of the background features was also considered, and their trans-
 193 formations are more likely to lie in a low dimensional sub-space and can thus be represented as a

194 low-rank matrix. After transformation, the method is more sensitive to color changes in saliency
 195 detection. The reader should refer to [6] for more details on the determination of \mathbf{T} .

196 3.3 Saliency refinement

The saliency of each pixel is temporarily assigned the saliency value of the superpixel of which it is a member, in other words, the saliency values are taken at superpixel level, as shown in Figure 3 (d), and are obtained by determining \mathbf{S} of Eqn.9. Further refinement is then required in order to assign the saliency value at pixel level by employing a bilateral filter [6], since it is more robust to imaging noise and the variation of imaging resolution and scale. That is, the saliency value \mathbf{S}'_u of each image pixel u is estimated as the weighted average of the saliency values of other pixels v :

$$\mathbf{S}'_u = \sum_{v=1}^T w_{uv} \mathbf{S}_v, \quad (10)$$

197 where T is the total number of pixels in the image, \mathbf{S} is the saliency map at superpixel level, and
 198 the Gaussian weight w_{uv} is defined as $w_{uv} = \frac{1}{Z_u} \exp(-\frac{1}{2}(\alpha\|\mathbf{c}_u - \mathbf{c}_v\|^2 + \beta\|\mathbf{p}_u - \mathbf{p}_v\|^2))$, where Z_u is
 199 defined in similar manner to Z_i^D above. A weighted Gaussian filter which considers both color and
 200 position is applied to the saliency map \mathbf{S} at superpixel level, in order to achieve the translation
 201 of per-superpixel saliency to per-pixel saliency. The trade-off between intensity and position is
 202 controlled by parameters α and β , both of which were set to 0.01 in the present work. The final
 203 saliency map highlights salient object regions of interest by suppressing the background of the
 204 image. Figure 3 (e) demonstrates the performance of this saliency refinement, and the property of
 205 human vision by which attention declines as the edge of the area of interest is approached may be
 206 mimicked.

207 3.4 Post-processing

208 The exact contours of the lesions can be finally extracted from the generated saliency map after
 209 removing confounding structures such as blood vessels, the optic disc, and the macular. The
 210 following steps are applied.

211 *Blood vessel segmentation:* We used the infinite perimeter active contour with hybrid region
 212 (IPACHR) method [39] to extract the retinal vasculature. IPACHR introduces a novel active
 213 contour model, and has the superior power in segmenting components with irregular and oscillatory

214 boundaries [40]. In addition, IPACHR considers both vesselness map based on local phase and
215 intensity of an image, so as to further improve the segmentation performance compared to the
216 typical infinite perimeter active contour model.

217 *Optic disc detection:* Usually, it has been well observed that any region with several surrounding
218 vessels greater than a threshold of 5 [41] will be assumed to be the optic disc, and will be removed.
219 In our experiments this method is efficient and effective. However, other sophisticated optic disc
220 detection methods [42, 43] may work equally well.

221 *Macular detection:* The macular region can be masked out by using the Gaussian Mixture
222 Model (GMM) proposed by [44]. Note, the source codes with default parameter settings provided
223 by the authors for these methods were used.

224 4 Datasets and Evaluation Metrics

225 To evaluate its effectiveness, we have evaluated the proposed method on seven publicly-available
226 retinal image datasets showing diabetic or malarial pathogenesis. These were: the Retina Check
227 project managed by Eindhoven University of Technology (RC-RGB-MA) [4]; the DiaretDB1 [45];
228 the Retinopathy Online Challenge training set (ROC) [46]; the e-optha [47]; the Messidor [48]; the
229 Diabetic Macular Edema (DME-DUKE) [27] dataset collected by Duke University; and the Malarial
230 Retinopathy dataset collected by the University of Liverpool (LIMA) [41]. Table 1 summarizes
231 the key information of these datasets. To achieve a single set of parameters, all the images from
232 different datasets were uniformly down-sampled to 768×768 . Note, the ground truth type of
233 lesion level indicates that the manual annotation was made by using a single pixel (center of the
234 lesions) or a coarse boundary (a disc could cover the entire lesion region); Image level shows that
235 the ground truth is graded as presence or absence of lesions; Pixel level reveals that the ground
236 truth is marked by labeling a precise contour of the lesion regions. The first five datasets are retinal
237 color fundus image, while the rest are fluorescein angiogram.

238 Two experts used an annotation tool to locate candidate MAs in RC-RGB-MA, and their
239 consensus was used for evaluation. Four experts annotated the MAs, HAs, and EXs indepen-
240 dently for DiaretDB1 by drawing a disc over the lesions, and reported confidence levels $\{< 50\%, \geq$
241 $50\%, 100\%\}$. The consensus of agreement higher than 75% was used to assign a region as a lesion.

242 For the ROC dataset, four experts indicated the center location of the MAs, and the logical OR was
243 used to combine the lesion locations and mark them as MAs. The MAs and EXs in e-optha were
244 manually annotated by an ophthalmologist who marked the lesion contours: a second ophthalmol-
245 ogist checked these annotations. The Messidor dataset was annotated regarding two significant
246 criteria: retinopathy grade, and risk of macular edema. For more details of grade criteria, we refer
247 the readers to [5]. The leakage contours of the DME-DUKE dataset were manually annotated by
248 two independent graders and later reviewed for intra-observer reliability. For the LIMA dataset,
249 one grader defined the boundaries of each large focal leak, and a second grader checked these
250 annotations.

251 The evaluations of these datasets were undertaken in three different ways, based on the types
252 of available manual annotations. A lesion-based approach defined candidate lesions and counted
253 them; a pixel-based approach focused on the location of lesions; and the image-based approach
254 aimed simply to determine whether a lesion was present.

255 To compare the detection results of the proposed method with their corresponding manual
256 annotations by human graders, the following metrics were employed: *sensitivity* (SE) = $TP/(TP+$
257 $FN)$, *specificity* (SP) = $TN/(TN + FP)$, and the area under the ROC curve (AUC), where TP ,
258 TN , FP and FN indicate true positive (correctly identified lesion pixels or regions), true negative
259 (correctly identified background pixels or regions), false positive (incorrectly identified lesion pixels
260 or regions), and false negative (incorrectly identified background pixels or regions), respectively.

261 5 Experimental Results

262 Once the saliency map has been generated, a threshold value $T = 0.65$ (which achieved the highest
263 AUC scores) was applied to the saliency map to obtain the candidate lesion regions for all the
264 datasets. Large blood vessels, the macular and the optic disc may also be enhanced as candidate
265 lesion regions or region of interest (ROI), as these regions are conspicuous objects in retinal images,
266 and can easily be distinguished visually by their intensity or shape, as shown in Figures 4-7. True
267 retinal lesions can be identified by simply masking away the blood vessels and the optic disc from
268 the produced saliency map. Figure 3 (f) shows the extracted lesion regions.

269 In these subsections, the performance of the proposed method is rigorously validated for the

270 detection of dark lesions and bright lesions.

271 5.1 Dark lesion detection

272 A large number of studies, i.e., ([3, 31, 25]) have performed lesion detection on prevalence of
273 referable at image level, but it is difficult to understand the criteria for selecting true positives and
274 false negatives. In the study of MA detection, the sensitivity values against the average number of
275 false positives per image (FPI) was used to measure performance [46]. It was obtained by averaging
276 the sensitivities taken at 7 points along the free-response receiver operating characteristic curve.
277 Sensitivity values for FPI rates of 1/8, 1/4, 1/2, 1, 2, 4, and 8 were thus obtained. A final score (FS)
278 was computed by averaging the sensitivity values obtained at these seven predefined FPIs [49]. The
279 sensitivity indicates the proportion of MAs correctly detected, and the FPI represents the number
280 of non-MAs incorrectly detected as MAs. Figures 4 (b) and (d) show that the proposed method
281 successfully detected the MA regions as salient. The exact MA regions could then be located after
282 removing other ROIs. Table 2 compares the MA detection performances of different methods in
283 terms of sensitivity against FPI on the e-optha, ROC, DiaretDB1, and recent released RC-RGB-
284 MA datasets respectively. For brevity, we provide readers with the performance only from the
285 three most recent MA detection methods (note, only [4] reports the detection performance on the
286 RC-RGB-MA dataset): this is not intended to be taken as exhaustive. As observed, the proposed
287 method outperforms the existing state-of-the-art ones on all the four datasets in terms of final
288 score.

289 Figure 5 demonstrates the ability our method to detect HE on two randomly selected images
290 from DiaretDB1 and Messidor datasets. In contrast to the MA detection, the HE detection has
291 received relatively little attention [33, 32, 50], and in the literature performance has been evaluated
292 only on DiaretDB1. Table 3 reports the sensitivity values achieved by different methods on the
293 DiaretDB1 dataset. Evaluation was undertaken at image and pixel level respectively. It can be seen
294 that the proposed method achieves the best performance at both the image and lesion levels with
295 the highest sensitivity values of 0.981 and 0.790 respectively. While both the deep-learning based
296 approaches [33, 32] focus on the detection of class-specific discriminative regions, the downsampling
297 operator in their architecture results in loss of location information, and the upsampling operator
298 tends to produce a coarse feature map that renders the fine grained lesion localization impossible.

299 Different types of dark lesions (MA and HE) may appear in a single retinal image. Therefore, a
300 comparative analysis of different methods in their detection is shown in Table 4. It can be observed
301 that the proposed method has a favorable detection performance compared to the existing ones.
302 To be more specific, the proposed method has produced a sensitivity value of 0.978, specificity of
303 0.955, and AUC of 0.964 on the DiaretDB1 dataset (at image level). It may be observed that our
304 *SE* score of dark lesion detection is lower than HE only detection in Table 3. This phenomenon
305 suggests that the combination of multiple lesions is more challenging to detect.

306 5.2 Bright lesion detection

307 The presence of exudates has been used to grade the risk of macular edema. Therefore, it is
308 important to detect and validate the presence of exudate. We evaluate the exudate detection
309 performance through the DiaretDB1, e-optha, and Messidor datasets. Both the DiaretDB1 and
310 e-optha datasets provide a lesion map generated by experts. While the Messidor dataset does not
311 manually annotate exudate contours, it provides a DR severity grading and contains information
312 on the risk of macular edema for each image.

313 Figure 6 depicts the saliency and exudate detection results of the proposed method over the
314 images from Messidor, DiaretDB1 and e-optha respectively. Table 5 shows the SE, SP and AUC
315 values of different methods. The proposed method achieves higher sensitivity, specificity, and AUC
316 values over DiaretDB1, e-optha, and Messidor when compared with the existing ones. It produced
317 the highest AUC scores of 0.952, 0.950, and 0.941, respectively. Our method exhibits superior
318 performance on DiaretDB1. For example, the sensitivity score of the method by Roychowdhury et
319 al. [13] would drop to 0.742 in order to achieve the same specificity score of 0.980. Even though
320 the sensitivity score of Agurto’s method reaches 1.000, its specificity score is only 0.730, which is
321 much lower than 0.950 by our method. It is worth noting that the AUC scores obtained by Zhang
322 [31] were computed at image level (presence of exudate).

323 In contrast to the large number of studies on detecting various lesions (MA, HE, and EX),
324 relatively few methods have been proposed for automated detection of leakage. Leakage in an-
325 giography is an important sign for clinicians to determine the relative activity and progression
326 of the underlying disease. In this work, performing the proposed method on leakage detection
327 was obtained over two FA image datasets: DME-DUKE with DR pathology, and LIMA with MR

328 pathology: Figure 7 shows one example from each. Table 6 shows the performances of different
329 methods in detecting leakage sites in terms of sensitivity, specificity, and AUC at pixel level. It
330 can be observed that the performances of our proposed method are again significantly better than
331 those compared ones.

332 **6 Discussion and Conclusion**

333 The extensive validation of the proposed retinal lesion detection method on seven publicly accessible
334 datasets with different pathologies and imaging modalities demonstrates its high potential to be
335 a powerful tool in the analysis of a wide spectrum of eye diseases. In this section, the method is
336 further investigated in terms of saliency analysis, saliency cues and feature importance.

337 **6.1 Comparison to the state-of-the-art saliency detection methods**

338 In the past decade, many saliency detection methods have been proposed. To decide which of
339 the saliency detection methods is superior when applied to retinal images, a comparison was
340 made between five state-of-the-art saliency detection methods regarding candidate lesion detection:
341 the classic saliency detection method proposed by Itti et al. [7], spectral residual saliency [51],
342 frequency-tuned saliency [52], graph-based visual saliency [53] and context-aware saliency [54].
343 The competitors are referred to here as IT, SR, FT, GB, and CA, respectively. The source codes,
344 with default parameter settings provided by the authors, were used for all these methods.

345 Figure 8 depicts saliency detection results by six methods over two images. The proposed
346 method identifies more comprehensive areas of saliency, which is consistent with the results ob-
347 tained by human visual inspection - both dark and bright lesions are highlighted as salient. The
348 SR method has the poorest performance, since spatial information is absent in the Fourier repre-
349 sentation, where the Fourier domain spectral energies derived from frequency bands alone are not
350 sufficient. The proposed model is not only capable of suppressing background, but also highlights
351 all salient regions (e.g., lesions, vessels, and the optic disc) with well-defined boundaries. By uti-
352 lizing the UNICOM feature, the proposed method can better handle the issues of heterogeneous
353 objects, poor contrast between object and background, large-scale and small-scale salient objects
354 more effectively compared with other saliency detection ones.

355 To evaluate the saliency detection performance objectively, the FPR and TPR of the saliency
356 maps derived by different methods were calculated. The ROC curves were obtained by varying
357 the threshold value in increments of 0.01 in $[0, 1]$, and observing the variation in SE versus (1-SP)
358 each time. The evaluations were undertaken for the detection of dark and bright lesions separately
359 across the aforementioned seven datasets. The averaged results of our method and its competitors
360 are plotted in Figure 9 (a). It can be seen that our method achieves the best performance for both
361 dark and bright lesion detection.

362 **6.2 Effectiveness of each saliency cue**

363 To validate the effectiveness of saliency cues in the proposed low-rank-based saliency analysis
364 method, we generated three receiver operating characteristics curves of the proposed method tak-
365 ing different cues: uniqueness cue only; compactness cue only; and combined uniqueness and
366 compactness cues (UNICOM).

367 The ROC curves in Figure 9 (b) show that the UNICOM feature performs better than either the
368 uniqueness or compactness feature alone. The proposed method combines uniqueness of intensity
369 and spatial distribution with the compactness of the image component, as a global constraint on
370 the saliency representation: the lesion regions have particular color (intensity) and shape (spatial)
371 characteristics. The uniqueness cue evaluates how different each respective element is from all the
372 other ones in an image, essentially measuring the relative ‘rarity’ of each element. The uniqueness
373 cue is also able to detect high similarity between multiple regions in the image and to suppress
374 globally repeated features. The compactness cue renders unique elements more salient when they
375 are grouped in a particular image region, rather than evenly distributed over the whole image. The
376 compactness cue is effective in distinguishing a salient region against background. The UNICOM
377 feature combines the complementarity of uniqueness and compactness measures for a more powerful
378 representation of saliency.

379 **6.3 Feature importance analysis**

380 In this section, the importance of the extracted features is investigated, to show the relative
381 contribution of different features to saliency analysis and lesion detection. Totally a set of 31
382 features were stacked vertically to form a feature vector, as shown in Table 7. We measured

383 the AUC scores 31 times for each dataset, omitting each factor in turn from the stacked feature
384 vector for saliency detection via the low-rank matrix recovery. The importance score was estimated
385 as $IS = 1 - SF_n$, where SF_n indicates the AUC score when feature F_n was excluded from the
386 stacked feature vector for saliency analysis and lesion detection. The importance scores were then
387 normalized into $[0, 1]$, where 1 indicates that the feature has the greatest effect on lesion detection,
388 and 0 shows that the feature does not effect on detection performance. Again, the analysis was
389 undertaken over two separate tasks: detection of bright and dark lesions. The obtained feature
390 importance maps are shown in Figure 10. As expected, the results demonstrate that the uniqueness-
391 based, compactness-based and UNICOM features are the most important descriptors among these
392 31 features, as illustrated in green in Figure 10.

393 6.4 Conclusions

394 Developing the proposed method was motivated by medical demands for effective tools to quantify
395 different types of lesions in retinal images. The accurate detection of retinal lesions is a challenging
396 problem due to variations across patients, image intensity inhomogeneity, irregular shape and
397 appearance of lesions., a novel low-rank-based saliency detection method was proposed to address
398 this challenge, based on the novel UNICOM feature derived from the global intensity and spatial
399 distribution of superpixels of the image.

400 Our extensive literature review shows that a single reliable method for automated detection
401 of multiple lesions at pixel level is relatively unexplored. To the best of our knowledge, this is
402 the first study on a new technique that is capable of the automated detection of hemorrhages,
403 microaneurysms, exudates, and leakage from both CF and FA images. The experimental results,
404 based on seven publicly-accessible DR and MR datasets, show that our method outperforms the
405 most recent alternative methods. The proposed method is not only capable of identifying the
406 presence of lesions in an image, but also can accurately locate and measure the size of such lesions.

407 It is interesting to note that the evaluation metrics demonstrate that our method has better
408 performances than the recent attention attracting deep learning-based approaches [33, 32]. It is
409 believed that while the latter focuses on the detection of class-specific features and high classifica-
410 tion accuracy, its architecture essential downsampling and upsampling operators imply that it has
411 inherent difficulty in determining the exact location of the features in the original images and thus

412 poor performance in detecting lesion regions at pixel level.

413 As shown in Figure 11, our saliency-driven method can detect both dark and bright lesions with
414 no complicated parameter tuning or training data collection. These lesions may be distinguished
415 by measuring the object size (which separates the MA from the HE), or intensity value (which
416 discriminates between the dark and bright lesions). As may be observed from Figure 11, the
417 proposed method is able to detect the vasculature, optic disc, macular, and abnormalities as
418 salient regions. It is therefore possible that in future work our method might be adapted for other
419 challenging tasks such as retinal vessel segmentation, optic disc detection and macular extraction.
420 Therefore, with the superior performance that we have demonstrated in this paper, it is our belief
421 that the proposed method will be a significant contribution to health informatics and will provide
422 a powerful tool for retinal image analysis and beyond with great potential for improved healthcare
423 and patient benefit.

424 7 Acknowledgment

425 This work was supported by National Science Foundation Program of China (61601029), Zhe-
426 jiang Provincial Natural Science Foundation (LZ19F010001), Ningbo Natural Science Foundation
427 (2018A610055), Grant of Ningbo 3315 Innovation Team.

428 8 Conflict of Interest

429 The authors have no relevant conflicts of interest to disclose.

430 References

- 431 [1] Niemeijer M., Abramoff M. D., Ginneken B.. Image structure clustering for image qual-
432 ity verification of color retina images in diabetic retinopathy screening *Med. image anal.*
433 2006;10:888–898.
- 434 [2] MacCormick I., Beare N., Taylor T., et al. Cerebral malaria in children: using the retina to
435 study the brain *Brain*. 2014:2119-2142.

- 436 [3] Seoud L., Hurtut T., Cheriet F., Langlois J. M. Pierre. Red Lesion Detection Using Dynamic
437 Shape Features for Diabetic Retinopathy Screening *IEEE Trans. Med. Imaging.* 2016;35:1116–
438 1126.
- 439 [4] Dashtbozorg B., Zhang J., Huang ., Haar Romeny B. M.. Retinal Microaneurysms Detection
440 Using Local Convergence Index Features *IEEE Trans. Image Processing.* 2018;27:3300–3315.
- 441 [5] Pires R., Avila S., Jelinek H. F., Wainer J., Valle E., Rocha A.. Beyond Lesion-Based Diabetic
442 Retinopathy: A Direct Approach for Referral *IEEE J. Biomed. Health.* 2017;21:193–200.
- 443 [6] Shen X., Wu Y.. A unified approach to salient object detection via low rank matrix recovery
444 in *Proceedings of CVPR*:853–860 2012.
- 445 [7] Itti L., Koch C., Niebur E.. A model of Saliency-Based visual attention for rapid scene analysis
446 *IEEE Trans. on Pattern Anal. Mach.Intell.*. 1998;20:1254-1259.
- 447 [8] Koch C., Ullman S.. Shifts in selective visual attention: towards the underlying neural cir-
448 cuitry. *Human neurobiology.* 1985;4 4:219-27.
- 449 [9] Yuan Y., Wang J., Li B., Meng M.. Saliency Based Ulcer Detection for Wireless Capsule
450 Endoscopy Diagnosis *IEEE Trans. Med. Imaging.* 2015;34:2046–2057.
- 451 [10] Yan J., Zhu M., Liu Y.. Visual Saliency Detection via Sparsity Pursuit *IEEE Signal Process.*
452 *Lett.*. 2010;17:739–742.
- 453 [11] Ko B., Nam J.. Object-of-interest image segmentation based on human attention and semantic
454 region clustering *J. Opt. Soc. Am. A.* 2006;23:2462-2470.
- 455 [12] Zhao Y., Zheng Y., Zhao Y., et al. Uniqueness-Driven Saliency Analysis For Automated
456 Abnormalities Detection with Application to Retinal Diseases in *Proceedings of MICCAI*:109-
457 118 2018.
- 458 [13] Roychowdhury S., Parhi K.K.. DREAM: Diabetic Retinopathy Analysis Using Machine Learn-
459 ing *IEEE J. Biomed. Health.* 2014;18:1717–1728.
- 460 [14] Mansour R. F.. Evolutionary Computing Enriched Computer-Aided Diagnosis System for
461 Diabetic Retinopathy: A Survey *IEEE Reviews in Biomed. Eng.*. 2017;10:334-349.

- 462 [15] Fleming A. D., Philip S., Goatman K. A., Olson J.A., Sharp P. F.. Automated microaneurysm
463 detection using local contrast normalization and local vessel detection *IEEE Trans. Med.*
464 *Imaging.* 2006;25:1223–1232.
- 465 [16] Giancardo L., Mériaudeau F., Li Y., Tobin K. W., Chaum E.. Microaneurysm detection with
466 radon transform-based classification on retina images in *Proceedings of EMBC*:5939–5942 2011.
- 467 [17] Tang L., Niemeijer M., Reinhardt J. M., Garvin M. K., Abràmoff M. D.. Splat Feature
468 Classification With Application to Retinal Hemorrhage Detection in Fundus Images *IEEE*
469 *Trans. Med. Imaging.* 2013;32:364–375.
- 470 [18] Pereira C., Gonçalves L., Ferreira M.. Exudate Segmentation in Fundus Images Using an Ant
471 Colony Optimization Approach *Inf. Sci.*. 2015;296:14–24.
- 472 [19] Dai B., Wu X., Bu W.. Retinal microaneurysms detection using gradient vector analysis and
473 class imbalance classification *PLOS ONE.* 2016;11:1-23.
- 474 [20] Phillips R., Forrester J., Sharp P.. Automated detection and quantification of retinal exudates
475 *Graefes Arch Clin Exp Ophthalmol.* 1993;231:90-4.
- 476 [21] Walter T., Klein J., Massin P., Erginay A.. A contribution of image processing to the diagnosis
477 of diabetic retinopathy-detection of exudates in color fundus images of the human retina *IEEE*
478 *Trans. Med. Imaging.* 2002;21:1236-1243.
- 479 [22] Sánchez C. I., García M., Mayo A., López M. Isabel, Hornero R.. Retinal image analysis based
480 on mixture models to detect hard exudates *Med. image anal.*. 2009;13 4:650-8.
- 481 [23] Sánchez C. I., Niemeijer M., Isgum I., et al. Contextual computer-aided detection: Improving
482 bright lesion detection in retinal images and coronary calcification identification in CT scans
483 *Med. image anal.*. 2012;16 1:50-62.
- 484 [24] Welfer D., Scharcanski J., Marinho D.. A coarse-to-fine strategy for automatically detecting
485 exudates in color eye fundus images *Comp. Med. Imag. and Grap.*. 2010;34:228-35.
- 486 [25] Giancardo L., al. . Exudate-based diabetic macular edema detection in fundus images using
487 publicly available datasets *Med. Image Anal.*. 2012;16:216–226.

- 488 [26] Agurto C., Murray V., Yu H., et al. A Multiscale Optimization Approach to Detect Exudates
489 in the Macula *IEEE J. Biomed. Health.* 2014;18:1328–1336.
- 490 [27] Rabbani H., Allingham M., Farsiu S.. Fully automatic segmentation of fluorescein leakage in
491 subjects with diabetic macular edema *Invest. Ophthalmol. Vis. Sci.*. 2015;56:1482-1492.
- 492 [28] Zhao Y., Zheng Y., Liu Y., et al. Intensity and Compactness Enabled Saliency Estimation
493 for Leakage Detection in Diabetic and Malarial Retinopathy *IEEE Trans. Med. Imaging.*
494 2017;36:51–63.
- 495 [29] Liu Q., Zhou B., Ke W., Zhao G.. A location-to-segmentation strategy for automatic exudate
496 segmentation in colour retinal fundus images *Comp. Med. Imag. and Grap.*. 2017;55:78–86.
- 497 [30] Rocha A., Carvalho T., Jelinek H. F., Goldenstein S., Wainer J.. Points of Interest and
498 Visual Dictionaries for Automatic Retinal Lesion Detection *IEEE Trans. Biomed. Eng.*.
499 2012;59:2244-2253.
- 500 [31] Zhang X., Thibault G., Decencière E., et al. Exudate detection in color retinal images for
501 mass screening of diabetic retinopathy *Med. Image Anal.*. 2014;18 7:1026-43.
- 502 [32] Gondal W. M., Köhler J. M., Grzeszick R., Fink G. A., Hirsch M.. Weakly-supervised localiza-
503 tion of diabetic retinopathy lesions in retinal fundus images *Proceedings of ICIP.* 2017:2069-
504 2073.
- 505 [33] Quéllec G., Charrière K., Y.Boudi , Cochener B., Lamard M.. Deep image mining for diabetic
506 retinopathy screening *Med. Image Anal.*. 2017;39:178–193.
- 507 [34] Perazzi F., Pritch Y., Hornung A.. Saliency filters: Contrast based filtering for salient region
508 detection in *Proceedings of CVPR* 2012.
- 509 [35] Cheng M., Zhang G., Mitra N., , Hu S.. Global Contrast based Salient Region Detection in
510 *Proceedings of CVPR*:409-416 2011.
- 511 [36] Achanta R., Shaji A., Smith K., Lucchi A., Fua P.. SLIC Superpixels Compared to State-of-
512 the-art Superpixel Methods *IEEE Trans. Pattern Anal. Mach.Intell.*. 2012;34:2274-2282.

- 513 [37] Candès E. J., Li X., Ma Y., Wright J.. Robust Principal Component Analysis? *J. ACM.*
514 2011;58:11:1–11:37.
- 515 [38] Wright J., Ganesh A., Rao S., Peng Y., Ma Y.. Robust Principal Component Analysis: Ex-
516 act Recovery of Corrupted Low-Rank Matrices via Convex Optimization in *Proceedings of*
517 *NIPS:2080–2088* 2009.
- 518 [39] Zhao Y., Rada L., Chen K., Harding S., Zheng Y.. Automated vessel segmentation using
519 infinite perimeter active contour model with hybrid region information with application *IEEE*
520 *Trans. Med. Imaging.* 2015;34:1797-1807.
- 521 [40] Li C., Xu C., Gui C., Fox M. D.. Distance Regularized Level Set Evolution and Its Application
522 to Image Segmentation *IEEE Transactions on Image Processing.* 2010;19:3243-3254.
- 523 [41] Zhao Y., MacCormick I. J., Beare N., Harding S. P., Zheng Y.. Automated Detection of
524 Leakage in Fluorescein Angiography Images with Application to Malarial Retinopathy *Sci.*
525 *Rep..* 2015;5:e10425.
- 526 [42] Cheng J., al. . Superpixel Classification Based Optic Disc and Optic Cup Segmentation for
527 Glaucoma Screening *IEEE Trans. Med. Imaging.* 2013;32:1019-1032.
- 528 [43] Tobin K.W., Chaum E., Govindasamy V., Karnowski T.. Detection of anatomic structures in
529 human retinal imagery *IEEE Trans. on Med. Imag..* 2014;26:1729-1739.
- 530 [44] Akram M. Usman, Tariq Anam, Khan Shoab A., Javed M. Younus. Automated Detection
531 of Exudates and Macula for Grading of Diabetic Macular Edema *Comput. Methods Prog.*
532 *Biomed..* 2014;114:141–152.
- 533 [45] Kauppi T., Kalesnykiene V., Sorri I., et al. The DIARETDB1 Diabetic Retinopathy Database
534 and Evaluation Protocol in *Proceedings of BMVC* 2007.
- 535 [46] Niemeijer M., Ginneken B., M. D. Abramoff et al.. Retinopathy Online Challenge: Auto-
536 matic Detection of Microaneurysms in Digital Color Fundus Photographs *IEEE Trans. Med.*
537 *Imaging.* 2010;29:185–195.
- 538 [47] Decencire E., al. . TeleOphta: Machine learning and image processing methods for teleoph-
539 thalmology *IRBM.* 2013;34:196–203.

- 540 [48] Kandemir M., Hamprecht F. A.. Computer-aided diagnosis from weak supervision: A bench-
541 marking study *Comput. Med. Imag. Grap.*. 2015;42:44-50.
- 542 [49] Antal B., al. . An Ensemble-Based System for Microaneurysm Detection and Diabetic
543 Retinopathy Grading *IEEE Trans. Biomed. Eng.*. 2012;59:1720–1726.
- 544 [50] Zhou L., al. . Automatic hemorrhage detection in color fundus images based on gradual
545 removal of vascular branches in *Proceedings of ICIP*:399-403 2016.
- 546 [51] Hou X., Zhang L.. Saliency detection: A spectral residual approach. in *Proceedings of CVPR*:1-
547 8 2007.
- 548 [52] Achanta R., Hemami S., Estrada F., Susstrunk S.. Frequency-tuned salient region detection
549 in *Proceedings of CVPR*:1597-1604 2009.
- 550 [53] Harel J., Koch C., Perona. P.. Graph-based visual saliency in *Proceedings of NIPS*:545-552
551 2006.
- 552 [54] Goferman S., Zelnik-Manor L., Tal A.. Context-Aware Saliency Detection *IEEE Trans. Pat-*
553 *tern Anal. Machine Intell.*. 2012;34:1915–1926.
- 554 [55] Wu B., Zhu W., Shi F., Zhu S., Chen X.. Automatic detection of microaneurysms in retinal
555 fundus images *Comp. Med. Imag. and Grap.*. 2017;55:106–112.
- 556 [56] Wang S, Tang H, al. . Localizing Microaneurysms in Fundus Images Through Singular Spec-
557 trum Analysis *IEEE Trans. Biomed. Eng.*. 2017;64:990-1002.
- 558 [57] Haloi M., Dandapat S., Sinha R.. A Gaussian Scale Space Approach For Exudates Detection,
559 Classification And Severity Prediction *CoRR*. 2015;abs/1505.00737.

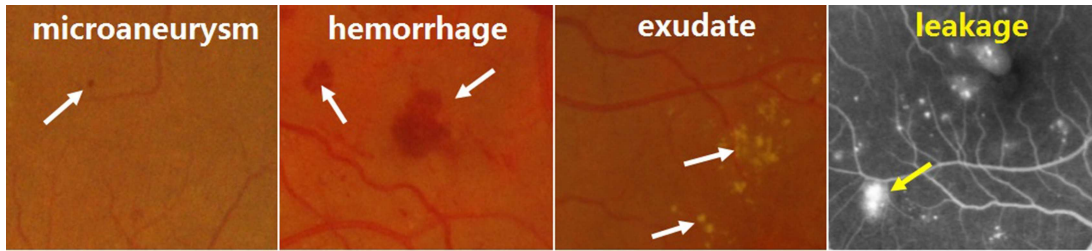


Figure 1: Four types of retinal abnormalities in color fundus and fluorescein angiography respectively.

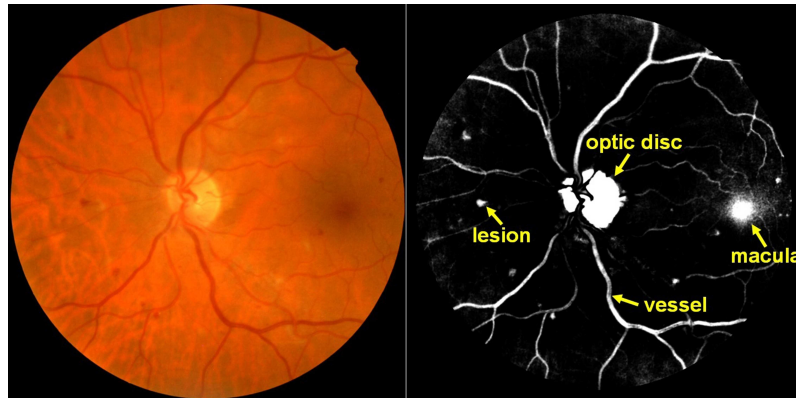


Figure 2: Examples of the proposed method on highlighting regions of interest (lesions, optic disc, vessel and the fovea) from an example retinal image.

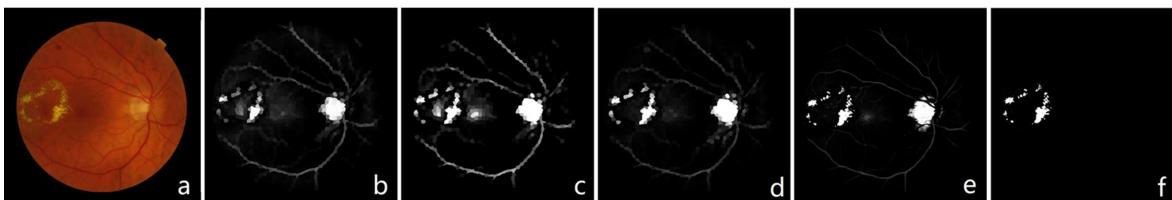


Figure 3: The main steps of the proposed method. (a) An example color fundus image; (b) Estimated uniqueness-based feature; (c) Estimated compactness-based feature; (d) Low-rank based saliency detection by using the combined uniqueness and compactness features; (e) Estimated saliency map at pixel-level; (f) Final lesion detection result after removing blood vessels, optic disc and macular regions.

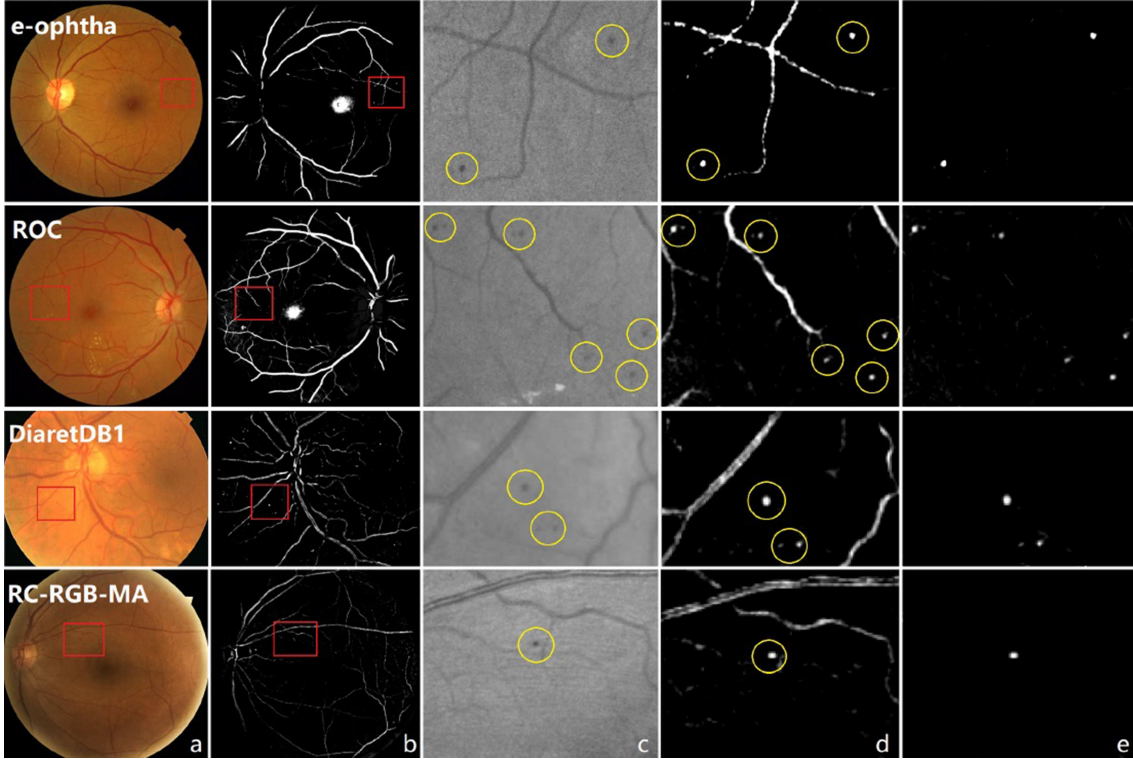


Figure 4: **Microaneurysm** detection results of the proposed method over four example images, one from each of four datasets. (a) Example images; (b) Saliency maps of (a); (c) Zoom-in view of the selected regions, and yellow circles indicate the locations of MAs; (d) Zoom-in view of saliency maps of the selected regions; (e) Detected MAs.

Table 1: Details of the retinal image datasets employed, and the values of controlling parameter k for each dataset.

Datasets	No. Img.	Size	FOV	Lesions	Disease	Groundtruth	Para. k
RC-RGB-MA	250	2595×1944	45°	MA	DR	Lesion level	6
DiaretDB1	89	1500×1152	50°	MA, HA, EX	DR	Lesion level	6
ROC	100	$768 \times 756 - 1394 \times 1392$	45°	MA	DR	Lesion level	7
e-ophta	195	$1440 \times 960 - 2544 \times 1696$	45°	MA, EX	DR	Pixel level	5
Messidor	1200	2304×1536	45°	MA, HA, EX	DR	Image level	-5
DME-DUKE	24	768×768	55°	LK	DR	Pixel level	-6
LIMA	30	$2189 \times 3061 - 3715 \times 2733$	50°	LK	MR	Pixel level	-6

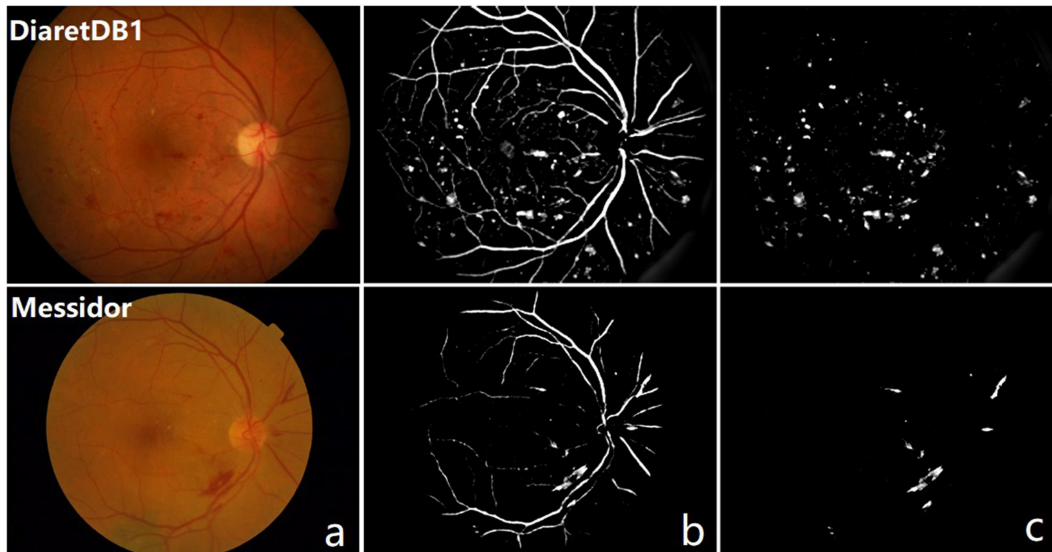


Figure 5: The **hemorrhage** detection results of the proposed method on two example images from the DiaretDB1 and Messidor dataset. (a) Original images; (b) Generated saliency map; (c) Detected hemorrhage regions.

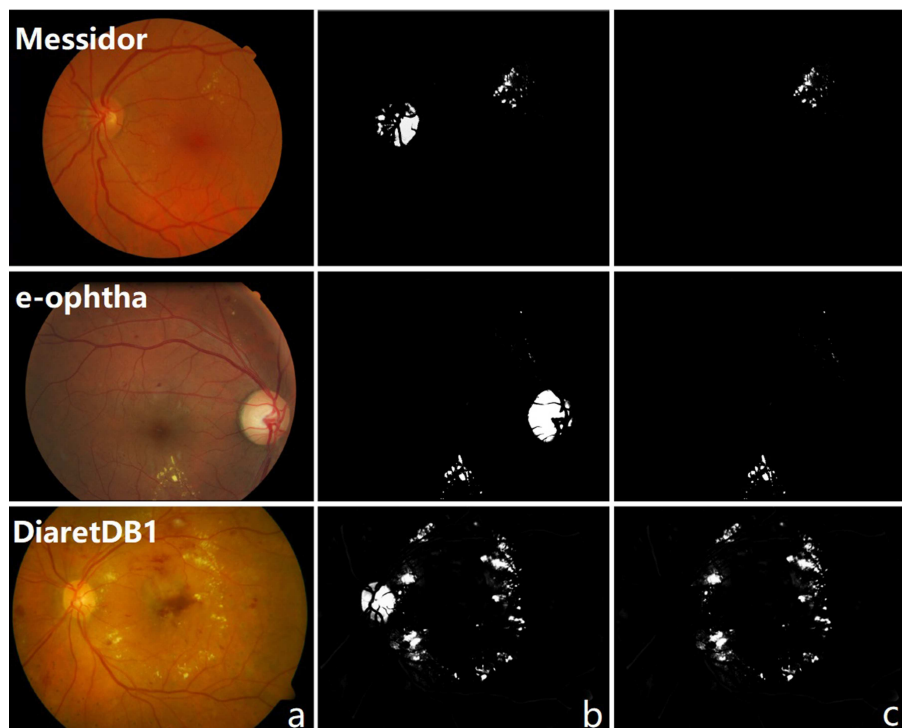


Figure 6: The detection results of **Exudate** using the proposed method in three example images, one from each of the three different datasets: (a) Example images; (b) Detected saliency; (c) Detected exudate regions.

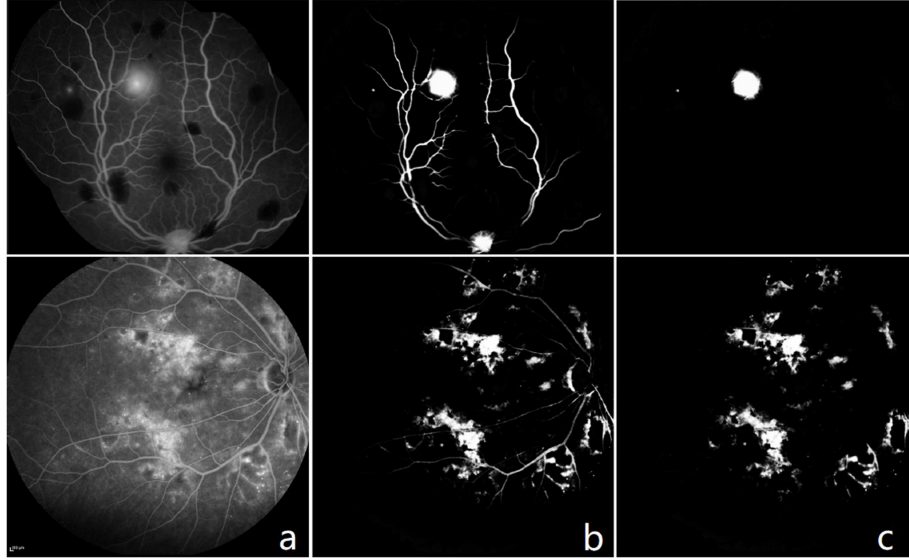


Figure 7: **Leakage** detection results of the proposed method on two example images from the LIMA and DUKE-DME datasets respectively. (a) Original images; (b) The generated saliency map; (c) Detected leakage regions.

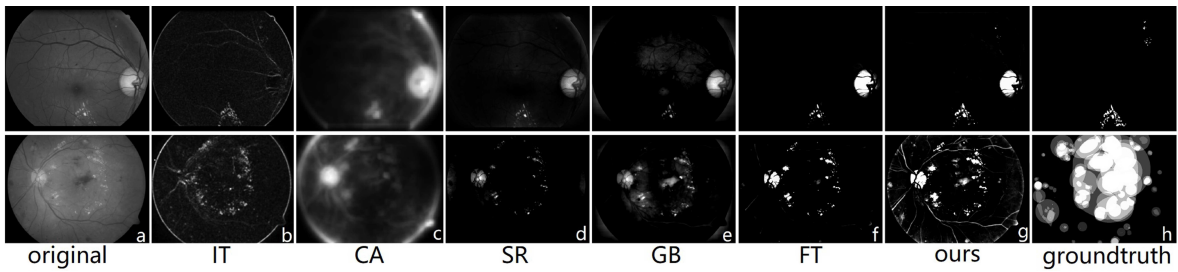


Figure 8: Saliency detection results of different algorithms over two example retinal images. (a) Original images. (b)-(g) Saliency maps generated using different methods. (h) Ground truth at lesion level: coarse lesion regions are annotated.

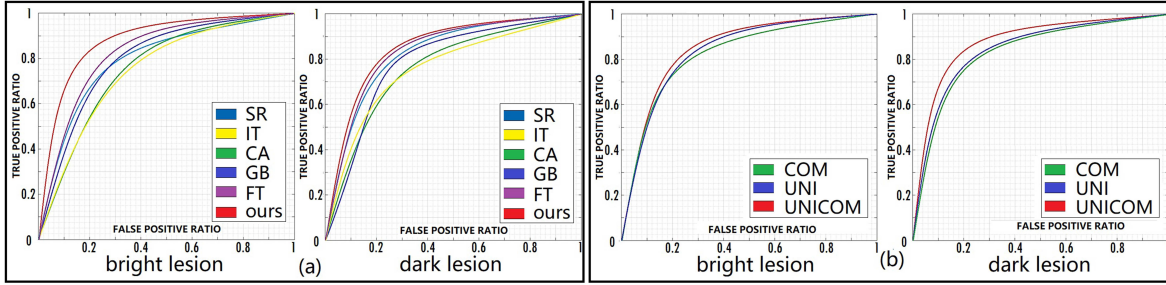


Figure 9: (a) Receiver operating characteristics curves of different saliency analysis methods for the detection of bright and dark lesions; (b) Receiver operating characteristics curves of the proposed method with different feature cues for the detection of bright and dark lesions respectively.

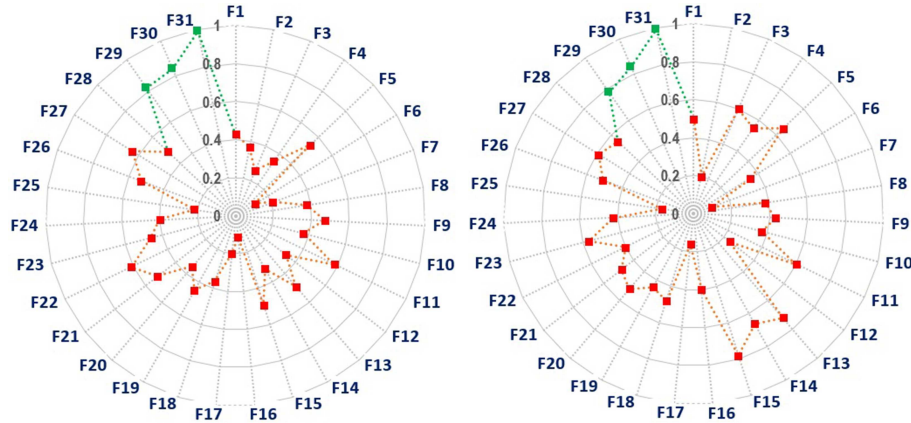


Figure 10: The relative importance of different features in the proposed method for the detection of different lesions. Left: bright lesion. Right: dark lesion.

Table 2: **Microaneurysms** detection result: Sensitivities of different methods at the predefined rates of false positives per image over four different datasets.

Dataset	Method	1/8	1/4	1/2	1	2	4	8	FS
e-ophta	Dashtbozorg et al. [4]	0.358	0.417	0.471	0.522	0.558	0.605	0.638	0.510
	Wu et al. [55]	0.063	0.117	0.172	0.245	0.323	0.417	0.573	0.273
	Zhang et al. [31]	0.170	0.240	0.320	0.440	0.540	0.630	0.740	0.440
	Proposed	0.325	0.387	0.443	0.501	0.551	0.637	0.738	0.512
ROC	Dashtbozorg et al. [4]	0.435	0.443	0.454	0.476	0.481	0.495	0.506	0.471
	Wang et al. [56]	0.273	0.379	0.398	0.481	0.545	0.576	0.598	0.464
	Wu et al.[55]	0.037	0.056	0.103	0.206	0.295	0.339	0.376	0.202
	Dai et al. [19]	0.219	0.257	0.338	0.429	0.528	0.598	0.662	0.433
Proposed	0.254	0.335	0.388	0.420	0.540	0.630	0.725	0.472	
DiaretDB1	Dashtbozorg et al. [4]	0.507	0.517	0.519	0.542	0.555	0.574	0.617	0.547
	Seoud et al. [3]	0.140	0.175	0.250	0.323	0.440	0.546	0.642	0.359
	Dai et al. [19]	0.035	0.058	0.112	0.254	0.427	0.607	0.755	0.321
	DRSCREEN [49]	0.001	0.003	0.009	0.020	0.059	0.140	0.257	0.070
Proposed	0.163	0.201	0.279	0.365	0.501	0.612	0.723	0.406	
RC-RGB-MA	Dashtbozorg et al. [4]	0.541	0.591	0.618	0.662	0.697	0.704	0.714	0.647
	Proposed	0.512	0.588	0.621	0.673	0.704	0.735	0.741	0.653

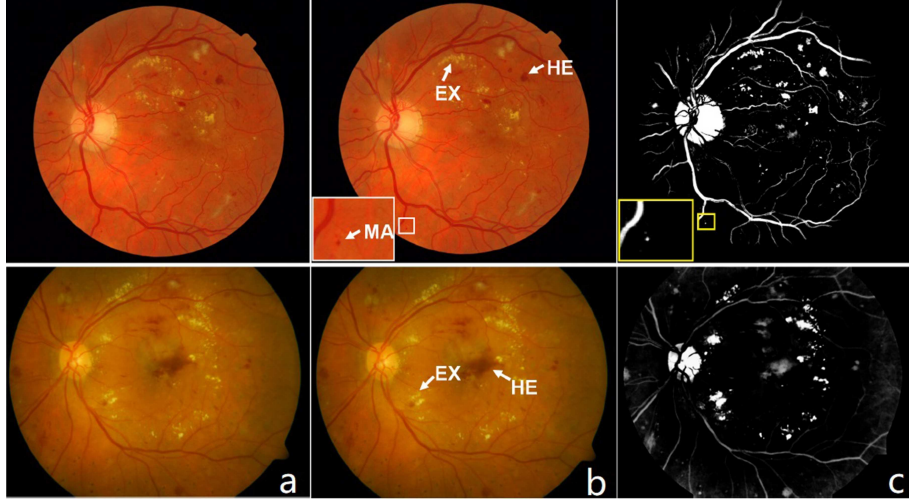


Figure 11: The detection results of different types of lesion regions by the proposed method: (a) Original images; (b) Manually annotated lesions; (c) Detected regions of interest.

Table 3: Sensitivity scores of different methods for the detection of **Hemorrhages** at image level and pixel level over the **DiaretDB1** dataset respectively. Note, the methods compared only reported their performances on sensitivity.

	Image level	pixel level
Quellec et al. [33]	0.947	0.710
Gondal et al. [32]	0.972	0.720
Zhou et al. [50]	0.944	-
proposed	0.981	0.790

Table 4: The SE, SP, and AUC values of different methods for dark lesion (hybrid of MA and HE) detection at image level over the **DiaretDB1** dataset.

	SE	SP	AUC
Kauppi et al. [45]	0.972	0.720	-
Roychowdhury et al. [13]	0.800	0.850	0.834
Rocha et al. [30]	0.900	0.830	0.933
Quellec et al. [33]	-	-	0.963
Proposed	0.978	0.955	0.964

Table 5: The SE, SP, and AUC values of different methods for the detection of **Exudates** over three different datasets.

Dataset	Method	SE	SP	AUC
DiaretDB1	Zhang et al. [31]	-	-	0.950
	Giancardo et al. [25]	0.860	0.850	0.953
	Quellec et al. [33]	0.809	-	-
	Walter et al. [32]	0.660	0.986	-
	Welfer et al. [21]	0.705	0.988	-
	Roychowdhury et al. [13]	0.742	0.980	-
	Liu et al. [29]	0.830	-	-
	Haloï et al. [57]	0.965	-	-
	Rocha et al. [30]	0.700	0.990	0.881
	Proposed	0.891	0.980	0.964
Messidor	Agurto et al. [26]	1.000	0.730	-
	Giancardo et al. [25]	-	-	0.900
	Zhang et al. [31]	-	-	0.930
	Rocha et al. [30]	0.900	0.640	0.893
	Proposed	0.912	0.950	0.941
e-ophta	Decencire et al. [47]	0.809	0.815	-
	Giancardo et al. [25]	-	-	0.870
	Zhang et al. [31]	0.830	-	-
	Proposed	0.856	0.910	0.895

* The evaluations were undertaken at lesion level for DiaretDB1, image level for Messidor, and pixel level for e-ophta.

Table 6: The SE, SP and AUC scores of different methods for the detection of **Leakage** over two different datasets.

Dataset	Method	SE	SP	AUC
DUKE-DME	Rabbani et al. [27]	0.690	0.910	0.800
	Zhao et al. [28]	0.780	0.940	0.860
	proposed	0.810	0.930	0.870
LIMA	Rabbani et al. [27]	0.810	0.870	0.840
	Zhao et al. [28]	0.930	0.960	0.940
	Proposed	0.950	0.950	0.950

Table 7: List of feature vectors for classification.

Feature notations	Descriptions
F_{1-5}	Max, min, mean, standard deviation, and entropy on intensity values of candidate patch in gray level.
F_{6-20}	Max, min, mean, standard deviation, and entropy on intensity values of candidate patch in R, G, B channels.
F_{21-23}	The color histogram of RGB, hue and saturation.
F_{24-28}	Max, min, mean, standard deviation, and entropy of the coordinates of centroid of candidate patch.
F_{29-31}	The proposed uniqueness-based, compactness-based and UNICOM feature.